

DOI: 10.1002/sml.200600562

# Nitrogen-Doped Tungsten Oxide Nanowires: Low-Temperature Synthesis on Si, and Electrical, Optical, and Field-Emission Properties

Mu-Tung Chang, Li-Jen Chou,\* Yu-Lun Chueh, Yu-Chen Lee, Chin-Hua Hsieh, Chii-Dong Chen, Yann-Wen Lan, and Lih-Juann Chen

**V**ery dense and uniformly distributed nitrogen-doped tungsten oxide (WO<sub>3</sub>) nanowires were synthesized successfully on a 4-inch Si(100) wafer at low temperature. The nanowires were of lengths extending up to 5 μm and diameters ranging from 25 to 35 nm. The highest aspect ratio was estimated to be about 200. An emission peak at 470 nm was found by photoluminescence measurement at room temperature. The suggested growth mechanism of the nanowires is vapor–solid growth, in which gaseous ammonia plays a significant role to reduce the formation temperature. The approach has proved to be a reliable way to produce nitrogen-doped WO<sub>3</sub> nanowires on Si in large quantities. The direct fabrication of WO<sub>3</sub>-based nanodevices on Si has been demonstrated.

## Keywords:

- doping
- field emission
- nanowires
- photoluminescence
- tungsten oxide


## 1. Introduction

In recent years, one-dimensional (1D) nanostructures and their fascinating properties and applications in nanodevices have attracted the attention of the scientific community. Compared to conventional materials, metal oxide nanowires, such as MgO,<sup>[1]</sup> ZnO,<sup>[2]</sup> SnO<sub>2</sub>,<sup>[3]</sup> In<sub>2</sub>O<sub>3</sub>,<sup>[4]</sup> Ga<sub>2</sub>O<sub>3</sub>,<sup>[5]</sup> and CdO<sup>[6]</sup> nanowires, have demonstrated versatile applications in field-effect transistors (FETs), sensors, lasers, and light-emitting nanodevices.<sup>[7a,b]</sup> Attention is also focused on the ferroelectricity, superconductivity, and magnetic properties of nanowires. Sodium tungsten oxide (Na<sub>x</sub>WO<sub>3</sub>,

$x \approx 0.05$ ), in particular, possesses an onset temperature of superconductivity at 90 K and light-emitting properties that are of great importance in the function of electronic and optoelectronic nanodevices.<sup>[8]</sup> Other interesting properties of WO<sub>3</sub> nanowires include a high melting point, high electrochromic response, and semiconductor behavior.<sup>[9a,b]</sup>

The growth mechanisms of oxide nanowires include both the vapor–liquid–solid (VLS) and vapor–solid (VS) mechanisms.<sup>[10a–g]</sup> The VLS growth mechanism relies on a metal catalyst reaching the supersaturation state at elevated temperature. Once there is a temperature fluctuation, a nanowire can be grown from the metal catalyst at the tip area. In contrast, the VS growth mechanism occurs anisotropically and free of metal catalyst at the tip region. In previous studies, tree- and rodlike WO<sub>3</sub> nanostructures have been synthesized by several groups.<sup>[10a–c]</sup> Treelike nanowires were synthesized by heating W foil partly covered by SiO<sub>2</sub> at a high temperature.<sup>[10a]</sup> The growth mechanism was proposed to be VLS in which the tungsten plate is covered with potassium halide.<sup>[10b]</sup> WO<sub>3</sub> nanorods prepared by either use of carbon nanotubes as a template or growth directly on the tungsten tips in an oxygen atmosphere are other well-known synthetic approaches in which the growth model is

[\*] M.-T. Chang, Prof. L.-J. Chou, Y.-L. Chueh, Y.-C. Lee, C.-H. Hsieh, Prof. L.-J. Chen  
Department of Materials Science and Engineering  
National Tsing Hua University  
Hsinchu, Taiwan 300 (R.O.C.)  
Fax: (+886) 35-722-366  
E-mail: ljchou@mx.nthu.edu.tw  
Dr. C.-D. Chen, Y.-W. Lan  
Institute of Physics, Academia Sinica  
Nankang, 115 Taipei, Taiwan (R.O.C.)

 Supporting information for this article is available on the WWW under <http://www.small-journal.com> or from the author.

suggested to be a VS mechanism.<sup>[10c-g,11]</sup> In addition, WO<sub>3</sub> nanorods/nanobelts were synthesized on the silicon samples using a physical vapor deposition process, and chemical methods were useful approaches as well.<sup>[12a,b]</sup> Also, WO<sub>x</sub> nanowires were grown by the oxidation of a WC<sub>x</sub> film obtained by converting W<sub>2</sub>C nanowires.<sup>[13]</sup> Recently, Liu et al. fabricated tungsten oxide nanorods by thermally oxidizing a tungsten spiral coil in a low vacuum at low substrate temperatures. The advantage of their study is the control of phases by tuning the process temperatures.<sup>[14a,b]</sup>

The advantages of the present process are that high-quality WO<sub>3</sub> nanowires can be produced in large quantities on a 4-inch Si wafer by introducing the reducing gas ammonia (NH<sub>3</sub>). This novel approach provides an alternative way to synthesize high-quality tungsten oxide nanowires on a Si wafer. The growth of the WO<sub>3</sub> nanowires is conducted by the VS mechanism, in which tungsten oxide vapor can be generated by reducing the tungsten oxide source with NH<sub>3</sub> gas. Photoluminescence (PL) measurements show a strong emission peak at 470 nm at room temperature. Taking advantage of the mature integrated Si process, the growth of WO<sub>3</sub> nanowires on whole Si wafers at low temperature can greatly reduce operational costs. It also provides a possible shortcut in the direct fabrication of WO<sub>3</sub>-based nanodevices in Si circuitry.

## 2. Results and Discussion

Figure 1a shows a scanning electron microscopy (SEM) image of an as-prepared sample, which reveals that a high density of nanowires was uniformly distributed. The nanowires are of lengths extending up to 5 μm and diameters ranging from 25 to 35 nm. The highest aspect ratio was estimated to be 200. The nanowires exhibit a polygonal morphology with no metal catalyst found at the tip areas (inset, Figure 1a). Figure 1b shows the SEM image with a 90° tilted view, which reveals that the high-density nanowires are grown directly on the Si substrate without the presence of a buffer layer. The grazing incidence X-ray diffraction (GIXRD) spectrum (Figure 2) indicates that the phase of the nanowires is cubic WO<sub>3</sub>, with indexed peaks corresponding to 200, 220, 222, 400, 420, and 422 planes with the lattice constant of  $a = 0.7521$  nm. The phase details of WO<sub>3</sub> have been described in the literature.<sup>[15]</sup> The space group is similar to that of cubic ReO<sub>3</sub> (*Pm3m*). The synthesis of nanowires of the same WO<sub>3</sub> phase at temperatures higher than 950 °C has been reported by Wang et al.<sup>[16]</sup>

Figure 3a shows the transmission electron microscopy (TEM) image of a WO<sub>3</sub> nanowire with a diameter of 25.5 nm. The high-resolution TEM image in Figure 3b is a magnified view of the outlined region in Figure 3a, which reveals the single crystallinity of the nanowire with no evidence of defects. The two  $d$  spacings of 0.37 nm are identified to correspond to WO<sub>3</sub> {200} planes. The inset in Figure 3a is the corresponding selected-area diffraction (SAD) pattern with [001] zone axis. Based on the analysis of high-resolution TEM images and SAD patterns, it can be concluded that the growth direction of the WO<sub>3</sub> nanowires is

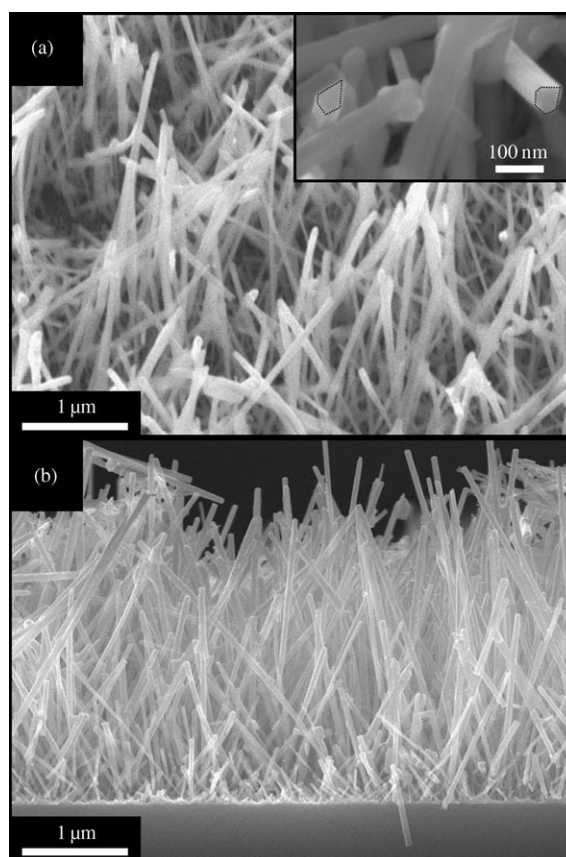


Figure 1. a) SEM image of WO<sub>3</sub> nanowires; inset: magnified view of part of the image. b) SEM image with view tilted at 90°.

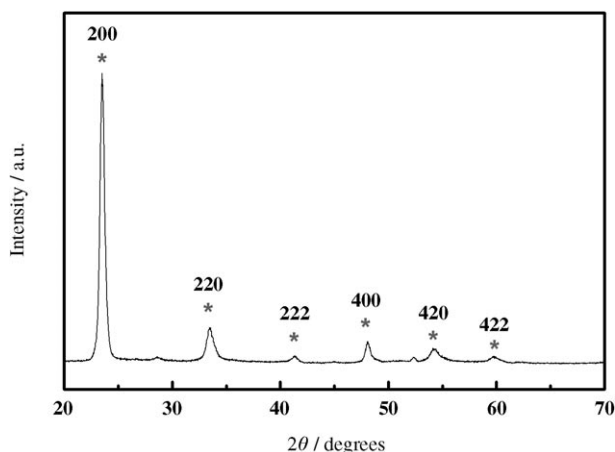
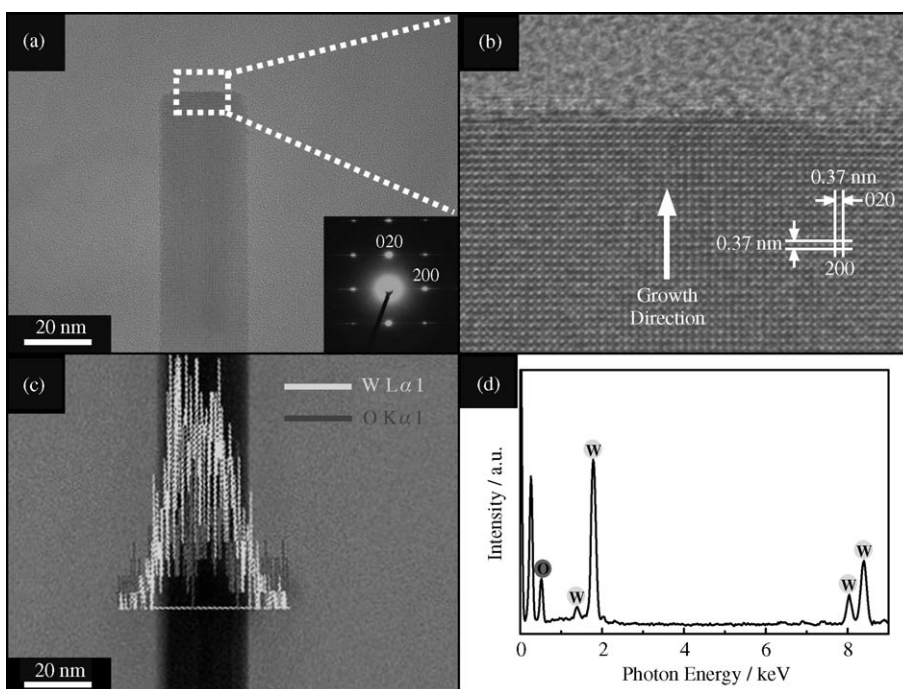


Figure 2. GIXRD spectrum of the WO<sub>3</sub> nanowires.

along the [010] direction, and the growth plane is the {100} plane. In Figure 3c, the corresponding elemental line-scan mapping of the nanowire obtained in the scanning TEM (STEM) mode indicates the atomic concentration of W and O to be 27 and 73%, respectively, which is estimated from the energy-dispersive spectrometry (EDS) data (Figure 3d) and is consistent with the appropriate atomic ratio of WO<sub>3</sub>.



**Figure 3.** a) TEM image of a nanowire; inset: the corresponding SAD pattern with the [001] zone axis. b) High-resolution TEM image of the WO<sub>3</sub> nanowire. c) The corresponding EDS elemental line profiles. d) Energy-dispersive spectrum with the atomic concentrations of W = 27% and O = 73%.

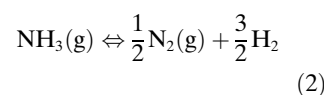
The X-ray photoelectron spectroscopy (XPS) results for the W 4f and O 2s core levels are shown in Figure 4a and b, respectively. The W 4f core-level value at 36 eV is very close to the reported value of 35.7 eV.<sup>[17]</sup> The small shoulder found in the O 2s spectrum can be fitted into two components at 530.5 and 532.5 eV (Figure 4b), and correspond to the binding energy of the WO<sub>3</sub> and the native oxide (SiO<sub>2</sub>) at the 1s core level according to ref. [18]. Nitrogen-doped WO<sub>3</sub> nanowires can be fabricated by the thermal decomposition of ammonia, which is confirmed by the X-ray photoelectron spectrum of nitrogen (Figure 4c). The concentrations of nitrogen in the nanowires are 1.61 and 2.75%, respectively, obtained by calculating the peak-height and peak-area ratios. The nitrogen peak in XPS (≈401 eV) is attributed to the dissolution of nitrogen inside the nanowires and no nitride phases, such as WN and W<sub>x</sub>(O, N) species, were found.<sup>[19]</sup>

In the present study, no metal catalysts were found at the tip regions, which suggests that the VS growth model is a more suitable explanation for this growth. In this model, the surface energy plays an important role in the growth of nanowires. The well-known two-dimensional (2D) nucleation probability was established as follows [Eq. (1)]:<sup>[20]</sup>

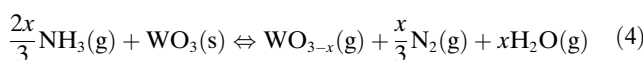
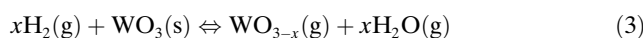
$$P_N = B \exp(-\pi\sigma^2/k^2T^2 \ln \alpha) \quad (1)$$

where  $P_N$  is the nucleation probability,  $B$  is a constant,  $\sigma$  is the energy of interaction between the nearest neighbors,  $k$  is the Boltzmann constant,  $T$  is absolute temperature, and  $\alpha$  is the supersaturation ratio, which is determined by  $\alpha = P/P_0$ .  $P$  and  $P_0$  are the actual vapor pressure and equilibrium vapor pressure, respectively, which are dependent on

the temperature  $T$ . Generally speaking,  $\alpha$  is usually larger than 1 at the supersaturation state. The solid W filament was first reacted with residual oxygen in the chamber to form the WO<sub>3</sub> phase, which is the most stable phase from a thermodynamic point of view.<sup>[21]</sup> On the other hand, ammonia gas can play a significant role in reducing the reaction temperature to generate tungsten vapor via decomposing the tungsten oxide on the surface of the tungsten filament. Ammonia gas is unstable and is easily decomposed to form N<sub>2</sub> and H<sub>2</sub> at 800 °C. The chemical reactions are suggested as follows [Eq. (2)]:<sup>[22]</sup>



The NH<sub>3</sub> and H<sub>2</sub> react with the WO<sub>3</sub> to produce the unstable tungsten oxide vapors as follows [Eqs. (3) and (4)]:



All the molecular species are condensed onto the nucleus through the rearrangement of the cation–anion complex to balance the local charge and structure on the Si substrate. During compositional and temperature fluctuations, the unstable tungsten oxide vapors are condensed and rearranged in the form of the 1D nanostructure with a stable and stoichiometric phase (WO<sub>3</sub>), thus allowing the nanowire to grow along the [010] direction, which is the fast growth direction of WO<sub>3</sub> nanowires. In addition, if we substituted the diluted hydrogen gas (H<sub>2</sub>/N<sub>2</sub> = 5%) for NH<sub>3</sub> at the same temperature, growth of nanowires could be achieved but the nanowires were nitrogen-free. However, no nanowires were found by only introducing N<sub>2</sub> gas. Therefore, we believe that the reducing gases play an imperative role in the growth of the 1D nanostructure. The process offers a convenient way to modify the electrical behavior and band structures of the tungsten oxide nanowires by using various reducing gases.

### 2.1. Electrical Measurements

Figure 5a shows a SEM image of the nanodevices investigated in the present study. The outer electrodes are la-

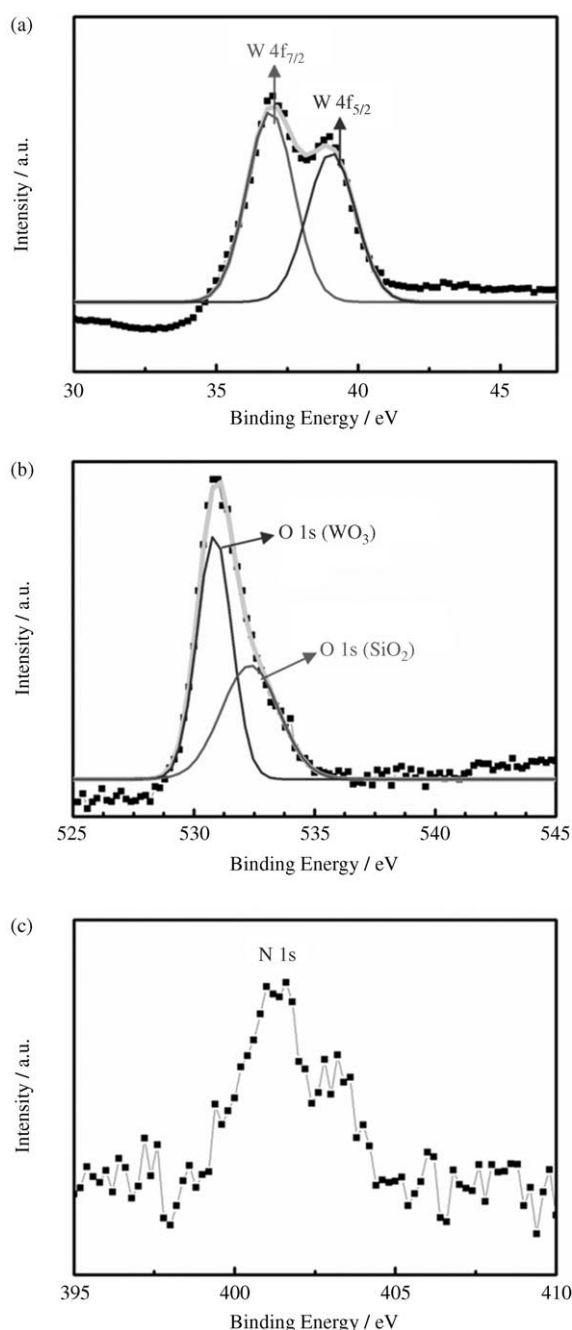


**Figure 4.** X-ray photoelectron spectra of the  $\text{WO}_3$  nanowires at the a) 4f core level of tungsten and b) 2s core level of oxygen. The curves are fitted based on the 2s core level of the  $\text{WO}_3$  and  $\text{SiO}_2$ , respectively. c) X-ray photoelectron spectrum at the nitrogen region.

beled 1 to 16 and the spacing of each electrode is 4  $\mu\text{m}$ . An enlarged image of part of the setup is shown in Figure 5b. Seven side-gate nanodevices were fabricated on the chip, but only three nanodevices were found to be functional for the study. This fact is attributed to a contact problem from the device processing, which results in an anomalous increase of the total resistance. Two-point current–voltage ( $I$ – $V$ ) measurements were performed in a LabView control-

led measurement system in air at room temperature. Figure 5c shows the  $I$ – $V$  characteristics measured from three devices labeled 02-03, 12-13, and 15-16 in Figure 5a. The linear  $I$ – $V$  curves indicate that the characteristics fit Ohm's law and the devices are good conductors. The zero-field resistances of the three nanodevices were measured to be 6.08, 7.31, and 2.79 k $\Omega$ , respectively. The measured resistances include the metal–nanowire contact resistance and the resistance of the nanowire itself. On the other hand, the measured total resistances are rather low, which indicates that the contact resistances are low as well. From Ohm's law, the resistivity of the nanowire can be calculated as  $\rho = (R \times A) / L$  ( $\rho$ : resistivity,  $R$ : resistance,  $A$ : cross-sectional area,  $L$ : length of nanowire). The diameters of the nanowires vary from 25 to 35 nm. Assuming that the  $\text{WO}_3$  nanowires are of circular cross section, the maximum resistivity obtained should vary by a factor of about  $(35/25)^2 \approx 1.96$ . The calculated resistivities of the nanodevices are listed in Table 1. The resistivity values are between  $3.36 \times 10^{-4}$  and

**Table 1.** Calculated resistivities of nanodevices and resistivities of tungsten oxides reported in refs. [28, 32].

Nanodevice	Resistance [k $\Omega$ ]	Resistivity [ $\Omega\text{cm}$ ]
02-03	6.08	$8.10 \times 10^{-4}$ – $1.59 \times 10^{-3}$
12-13	7.31	$1.15 \times 10^{-3}$ – $2.25 \times 10^{-3}$
15-16	2.79	$3.36 \times 10^{-4}$ – $6.59 \times 10^{-4}$
Single-crystal $\text{WO}_3$ nanowires		$3.36 \times 10^{-4}$ – $2.25 \times 10^{-3}$
Crystallized $\text{WO}_3$ film <sup>[23]</sup>		$8.8 \times 10^{-3}$
Amorphous $\text{WO}_3$ film <sup>[26]</sup>		$1.0 \times 10^6$

$2.25 \times 10^{-3} \Omega\text{cm}$ , which is an order of magnitude lower than that of the crystallized tungsten oxide thin films.<sup>[23]</sup> Although the values are considerably higher than those of metallic nanowires, such as NiSi (15  $\mu\Omega\text{cm}$ ) and  $\text{CoSi}_2$  (20  $\mu\Omega\text{cm}$ ) nanowires,<sup>[24a,b]</sup> the conductivity of the  $\text{WO}_3$  nanowires is superior to those of heavily n-doped Si ( $\approx 10^{20} \text{cm}^{-3}$ ) semiconductors (bulk).<sup>[25]</sup> This finding indicates that the  $\text{WO}_3$  nanowire is an outstanding candidate for nano-FET devices with considerably low resistivity.

From the electrical measurement data that comply with Ohm's law, it can be concluded that the resistivity of the nanowires does not seem to be dependent on their geometry and aspect ratio. Previous investigations on the electrical properties of tungsten oxide reported that the resistivity of amorphous tungsten oxide is about  $10^6 \Omega\text{cm}$  and that of the crystallized  $\text{WO}_3$  is about  $10^{-2}$ – $10^{-3} \Omega\text{cm}$ .<sup>[23,26a]</sup> The lower resistivity of  $\text{WO}_3$  nanowires compared with that of crystallized film is attributed to nitrogen doping as well as the single-crystal and defect-free nature of the nanowires. The optical bandgap of the tungsten oxide moves to a lower energy from the amorphous to the crystalline state (from 3.25 to 2.75 eV).<sup>[23,26a,b]</sup> The bandgap variation with the crystalline state may be responsible for the change of resistivity. In addition, the defects are scattering centers that may retard the transport of carriers. Thus, the nearly perfect crystalline structures of the nanowires lead to better electrical performance.

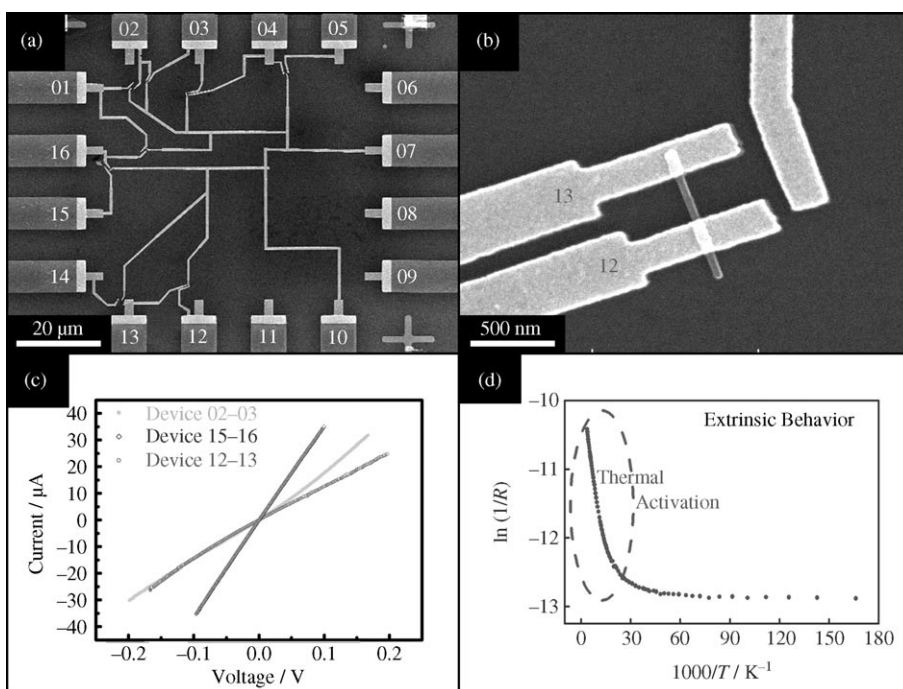


**Figure 5.** a) SEM image of nanodevices; b) enlarged image of the device formed with electrodes 12 and 13. c)  $I$ - $V$  characteristics measured from three different devices; and d) resistances measured at different temperatures.

In general, the electronic transport of  $\text{WO}_3$  is known to be governed by the hopping conduction mechanism and the electrons are the major carriers via the oxygen vacancies.<sup>[27]</sup> In this context, nitrogen doping in the present case can provide an acceptor site to compensate the electron. Figure 5d shows the temperature dependence of a single  $\text{WO}_3$  nanowire, which indicates the low-temperature behavior of a semiconductor. In addition, the linear curve ( $\ln(1/R) \approx 1000/T$ ) enclosed by the dotted line in Figure 5d suggests that the transport mechanism is dominated by thermal activation at high temperatures ( $\approx 25$ – $300$  K). The thermal-activation model predicts that the conductivity follows the equation  $\sigma(T) = \sigma_0 \exp(-\Delta E/k_B T)$ , where  $\sigma$  is the conductivity,  $k_B$  is the Boltzmann constant, and  $\Delta E$  is the activation energy. From the slope of the  $\ln(1/R) \approx 1000/T$  curve, an activation energy of  $\Delta E \approx 0.02$  eV is estimated. The extremely low activation energy implies that the carrier concentration is high and the dominant mechanism of carrier generation is an extrinsic behavior. On the other hand, in the low-temperature region ( $T < 25$  K),  $\ln(1/R)$  is independent of the temperature. This result indicates that the thermal-activation carriers are too low in number to affect the amount of the total carriers.

## 2.2. PL Spectrum of $\text{WO}_3$

Figure 6 shows the PL spectrum of  $\text{WO}_3$  nanowires excited by a He-Cd laser with a wavelength of 325 nm at room temperature. The strong peak was found at 470 nm. Note that emission through quantum confinement effects

can be ruled out because the diameter of the  $\text{WO}_3$  nanowires is larger than that of the critical radius. In the present study, the emission peak at 470 nm is possibly due to trap-state emission. In this case, each oxygen vacancy would trap one electron from the transition level of a tungsten atom to become an ionized oxygen vacancy. Since it is a reduction process, many oxygen vacancies are expected to form. Similar results attributed to oxygen-related defects were reported for ZnO and  $\text{Al}_2\text{O}_3$  nanowires.<sup>[28a,b]</sup> Meanwhile, W atoms, which contribute electrons to the trap state, tend to form the most stable oxide phase ( $\text{WO}_3$ ) to balance the cation-anion relationship.

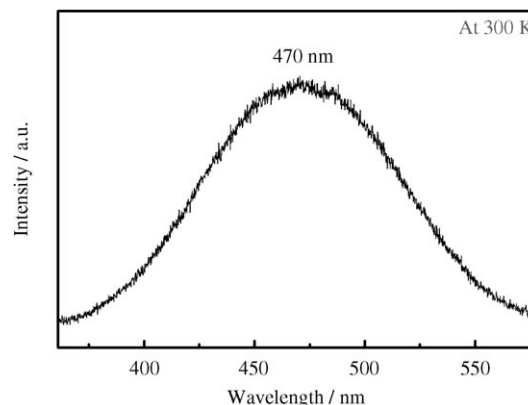


**Figure 6.** PL spectrum of the blue-green peak at a wavelength of 470 nm at room temperature.

## 2.3. Field-Emission Properties of $\text{WO}_3$

Figure 7 shows the relationship between the current density and applied field at separations of 100 and 150  $\mu\text{m}$  between the anode and samples. In general, the turn-on field and threshold field are defined as the electric field required for generating a current density of  $10 \mu\text{A cm}^{-2}$  and  $10 \text{ mA cm}^{-2}$ , respectively. From our repeated experiments, the tungsten oxide nanowires exhibit a turn-on field of  $6.44 \text{ V } \mu\text{m}^{-1}$  and a threshold field of  $9.42 \text{ V } \mu\text{m}^{-1}$  at an anode-sample separation of 100  $\mu\text{m}$ . The values are favorably comparable to those of many other semiconductor nanowires.<sup>[29a,b]</sup> The value of the turn-on field in our study is higher than the results previously reported for tungsten

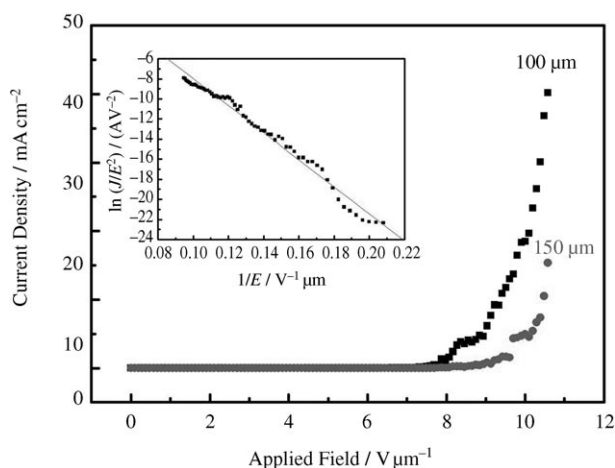


**Figure 7.** The electron field-emission behavior of tungsten oxide nanowires.

oxide nanowires.<sup>[10d,14a]</sup> The variations of the turn-on fields may be attributed to the differences in phases and chemical compositions. However, they are comparable with other functional metal oxides for potential application in field-emission devices. The maximum current density can be as high as  $40 \text{ mA cm}^{-2}$  (under an applied field of  $10.57 \text{ V } \mu\text{m}^{-1}$ ), which is comparable with some reports for carbon nanotube emitters.<sup>[30a,b]</sup> The inset of Figure 7 shows the corresponding Fowler–Nordheim plot  $[\ln(J/E^2)]$  versus  $1/E$ , and the Fowler–Nordheim relationship can be given as [Eq. (5)]:<sup>[31]</sup>

$$J = (A\beta^2 E^2 / \Phi) \exp(-B\Phi^{3/2} / \beta E) \quad (5)$$

where  $J$  is the current density,  $E$  is the applied field strength, and  $\Phi$  is the work function.  $A$  and  $B$  are constants corresponding to  $1.56 \times 10^{-10} [\text{AV}^{-2} (\text{eV})]$  and  $6.83 \times 10^3 [\text{V} (\text{eV}^{-3/2}) (\mu\text{m}^{-1})]$ , respectively. The field-enhancement factor  $\beta$  reflects the degree of field emission for the tip shape on a planar surface, and can be estimated from the slope  $(-B\Phi^{3/2}/\beta)$  of the Fowler–Nordheim plot, assuming the work function of  $\text{WO}_3$  to be  $5.7 \text{ eV}$ .<sup>[32a,b]</sup> Two straight lines can be unambiguously found and reflect the different  $\beta$  values at the high- and low-field regions. At the high-field region ( $E > 4.8 \text{ V } \mu\text{m}^{-1}$ ), the  $\beta$  value is equal to 691 (the correlation coefficient of linear curve fitting is  $-0.99129$ ). The variations of  $\beta$  can be ascribed to the degree of screening effect at the high- and low-field regions. The results indicate that the barrier-tunneling mechanism is responsible for the phenomenon of field emission.

### 3. Conclusions

We have shown that  $\text{WO}_3$  nanowires can be synthesized on a 4-inch silicon wafer. The nanowires are very dense and uniform with a length extending up to  $5 \mu\text{m}$  and diameters ranging from  $25$  to  $35 \text{ nm}$ . The highest aspect ratio was calculated to be 200. The growth model follows the VS mechanism with a growth direction of  $[010]$ . The electrical trans-

port properties show that the semiconducting  $\text{WO}_3$  nanowires possess very low resistivity, which indicates that they could be an outstanding contact material for nano-FET devices.

### 4. Experimental Section

Si wafers (4 in.) were chemically cleaned by a standard process and loaded into a vacuum chamber pumped to a vacuum of  $10^{-2}$  Torr. A tungsten filament with a diameter of several millimeters as the heater reacted with the residual oxygen during annealing to form a tungsten oxide source on the surface of the filament, which was fixed at a distance of about 3 mm above the substrate. Before the ammonia was introduced, the temperature of the wafer was increased to  $800^\circ\text{C}$  by passing a current through the filament (voltage 28 V, current 20 A). Subsequently, 5–10 sccm ammonia was introduced to the growth chamber to react with the filament for 20 min. After annealing, the samples were cooled to room temperature and their surfaces were covered completely with semitransparent, dark blue, powderlike films. GIXRD with a fixed incident angle of  $0.5^\circ$  was carried out to identify the phases. A field-emission transmission electron microscope (JEM-3000F, operated at 300 kV with a point-to-point resolution of 0.17 nm) equipped with an energy-dispersion spectrometer, an electron energy-loss spectrometer, and a high-angle annular dark-field detector was used to obtain information on the microstructures and chemical compositions. The surface morphology was examined with a field-emission scanning electron microscope (JOEL JSM-6500F) operated at 15 kV. The PL spectra were acquired with a He–Cd laser of wavelength 325 nm as the light source at room temperature. The electron field-emission behavior was measured in a vacuum of  $1 \times 10^{-7}$  Torr using a spherical stainless-steel probe (1 mm in diameter) as the anode. The area of the anode for effectively probing the field emission was  $0.0012 \text{ cm}^2$ . Electrical measurements were performed by sequential procedures including electrodes defined by electron-beam lithography, metal evaporation, and device evaluation. The sample with nanowires grown on the surface was tightly contacted with a designed pattern substrate with a common clip, followed by transferring the nanowire from the sample surface to the substrate by ultrasonic vibration. The field-emission scanning electron microscope (JOEL JSM-6500F) was used to locate the positions of the randomly dispersed nanowires on the chips. Ni (35 nm) and Au (65 nm) were selected as the contact electrode materials. The width of the electrodes on the nanowires was designed to be  $0.2 \mu\text{m}$ . A 30-kV cold field-emission scanning electron microscope (FEI-SIRION) with nanopattern generation system was used for this purpose. A LabView program was used to control the  $I$ – $V$  testing process.

## Acknowledgements

This research was supported by the National Science Council through grant no. NSC 94-2215-E-007-004 and the Ministry of Education through grant no. 94-E-FA04-1-4.

- [1] Y. Yin, G. Zhang, Y. Xia, *Adv. Funct. Mater.* **2002**, *12*, 293–298.
- [2] M. H. Huang, S. Mao, H. Feich, H. Yan, Y. Wu, H. Kind, E. Weber, R. Russo, P. Yang, *Science* **2001**, *292*, 1897–1902.
- [3] Z. R. Dai, J. L. Gole, J. D. Stout, Z. L. Wang, *J. Phys. Chem. B* **2002**, *106*, 1274–1279.
- [4] X. S. Peng, Y. W. Wang, J. Zhang, X. F. Wang, L. X. Zhao, G. W. Meng, L. D. Zhang, *Appl. Phys. A* **2002**, *74*, 437–439.
- [5] Y. C. Choi, W. S. Kim, Y. S. Park, S. M. Lee, D. J. Bae, Y. H. Lee, G. S. Park, W. B. Choi, N. S. Lee, J. M. Kee, *Adv. Mater.* **2000**, *12*, 746–750.
- [6] Y. Liu, C. Yin, W. Wang, Y. Zhan, G. J. Wang, *J. Mater. Sci. Lett.* **2002**, *21*, 137–139.
- [7] a) Z. R. Dai, Z. W. Pan, Z. L. Wang, *Adv. Funct. Mater.* **2003**, *13*, 9–24; b) Z. W. Pan, Z. R. Dai, Z. L. Wang, *Science* **2001**, *291*, 1947–1952.
- [8] A. Shengelaya, S. Reich, Y. Tsabba, K. A. Müller, *Eur. Phys. J. B* **1999**, *12*, 13–15.
- [9] a) W. Cheng, E. Baudrin, B. Dunn, J. I. Zink, *J. Mater. Chem.* **2001**, *11*, 92–97; b) D. Cummins, G. Boschloo, R. Michael, D. Corr, N. S. Rao, D. Fitzmaurice, *J. Phys. Chem. B* **2000**, *104*, 11449–11459.
- [10] a) Y. Q. Zhu, W. Hu, W. K. Hsu, M. Terrones, N. Grobert, J. P. Hare, H. W. Kroto, D. R. M. Walton, *Chem. Phys. Lett.* **1999**, *309*, 327–334; b) H. Qi, C. Wang, J. Liu, *Adv. Mater.* **2003**, *15*, 411–414; c) B. C. Satishkumar, A. Govindaraj, M. Nath, C. N. R. Rao, *J. Mater. Chem.* **2000**, *10*, 2115–2119; d) Y. Li, Y. Bando, D. Golberg, *Adv. Mater.* **2003**, *15*, 1294–1296; e) G. Gu, B. Zheng, W. Q. Han, S. Roth, J. Liu, *Nano Lett.* **2002**, *2*, 849–851; f) K. Liu, D. T. Foord, L. Scipioni, *Nanotechnology* **2005**, *16*, 10–14; g) Z. Liu, Y. Bando, C. Tang, *Chem. Phys. Lett.* **2003**, *372*, 179–182.
- [11] M. Feng, A. L. Pan, H. R. Zhang, Z. A. Li, F. Liu, H. W. Liu, D. X. Shi, B. S. Zou, H. J. Gao, *Appl. Phys. Lett.* **2005**, *86*, 141901-1–141901-3.
- [12] a) Y. B. Li, Y. Bando, D. Golberg, K. Kurashima, *Chem. Phys. Lett.* **2003**, *367*, 214–218; b) X.-L. Li, J.-F. Liu, Y.-D. Li, *Inorg. Chem.* **2003**, *42*, 921–924.
- [13] S.-J. Wang, C.-H. Chen, R.-M. Ko, Y.-C. Kuo, C.-H. Wong, C.-H. Wu, *Appl. Phys. Lett.* **2005**, *86*, 263103-1–263103-3.
- [14] a) J. Liu, Z. Zhang, Y. Zhao, X. Su, S. Liu, E. Wang, *Small* **2005**, *1*, 310–313; b) J. Liu, Y. Zhao, Z. Zhang, *J. Phys. Condens. Matter* **2003**, *15*, L453–L461.
- [15] A. R. Siedle, T. E. Wood, M. L. Brostrom, D. C. Koskenmaki, B. Montez, E. Oldfield, *J. Am. Chem. Soc.* **1989**, *111*, 1665–1669.
- [16] J. Zhou, Y. Ding, S. Z. Deng, L. Gong, N. S. Xu, Z. L. Wang, *Adv. Mater.* **2005**, *17*, 2107–2110.
- [17] O. Yu. Khyzhun, *J. Alloys Compd.* **2000**, *305*, 1–6.
- [18] F. Verpoort, A. R. Bossuyt, L. Verdonck, *J. Electron Spectrosc. Relat. Phenom.* **1996**, *82*, 151–163.
- [19] H. L. Zhang, D. Z. Wang, N. K. Huang, *Appl. Surf. Sci.* **1999**, *150*, 34–38.
- [20] N. Cabrera, W. K. Burton, *Discuss. Faraday Soc.* **1949**, *5*, 40–48.
- [21] <http://cea.grc.nasa.gov/>.
- [22] H. Lee, J. S. Harris, Jr., *J. Cryst. Growth* **1996**, *169*, 689–696.
- [23] K. H. Yoon, J. W. Lee, Y. S. Cho, D. H. Kang, *Appl. Phys. Lett.* **1996**, *68*, 572–574.
- [24] a) L. J. Chen, *JOM* **2005**, *57(9)*, 24–30; b) H. Okino, I. Matsuda, R. Hobara, Y. Hosomura, S. Hasegawa, *Appl. Phys. Lett.* **2005**, *86*, 233108-1–233108-3.
- [25] D. K. Schroder, *Semiconductor Material and Device Characterization*, 2nd ed., Wiley-Interscience, **1998**, p. 47.
- [26] a) K. Miyake, H. Kaneko, M. Sano, N. Suedomi, *J. Appl. Phys.* **1984**, *55*, 2747–2753; b) M. G. Hutchins, N. A. Kamel, N. El-Kadry, A. A. Ramadan, K. Abdel-Hady, *Phys. Status Solidi A* **1999**, *175*, 991–1002.
- [27] P. Kofstad, *Nonstoichiometry, Diffusion, and Electrical Conductivity in Binary Metal Oxides*, Wiley, New York, **1972**, p. 208.
- [28] a) X. S. Peng, L. D. Zhang, G. W. Meng, X. F. Wang, Y. W. Wang, C. Z. Wang, G. S. Wu, *J. Phys. Chem. B* **2002**, *106*, 11163–11167; b) Y. Dai, Y. Zhang, Q. K. Li, C. W. Nan, *Chem. Phys. Lett.* **2002**, *358*, 83–86.
- [29] a) Y. L. Chueh, L. J. Chou, C. A. Hsu, S. C. Kung, *J. Phys. Chem. B* **2005**, *109*, 21831–21835; b) Y. B. Li, Y. Bando, D. Golberg, *Appl. Phys. Lett.* **2003**, *82*, 1962–1964.
- [30] a) C. Y. Zhi, X. D. Bai, E. G. Wang, *Appl. Phys. Lett.* **2002**, *81*, 1690–1692; b) Y. Liu, S. Fan, *Solid State Commun.* **2005**, *133*, 131–134.
- [31] R. H. Fowler, L. W. Nordheim, *Proc. R. Soc. London Ser. A* **1928**, *119*, 173–181.
- [32] a) G. Vida, V. K. Josepovits, M. Gyor, P. Deak, *Microsc. Microanal.* **2003**, *9*, 337–342; b) M. Gillet, R. Delamare, E. Gillet, *Eur. Phys. J. D* **2005**, *34*, 291–294.

Received: October 13, 2006

Revised: November 23, 2006

Published online on February 22, 2007